Performance estimation by multiphase-field simulations and transmission-line modeling of nickel coarsening in FIB-SEM reconstructed Ni-YSZ SOFC anodes I: Influence of wetting angle

Paul W. Hoffrogge [a,*], Daniel Schneider [a,b], Florian Wankmüller [c,d], Matthias Meffert [d], Dagmar Gerthsen [d], André Weber [c], Britta Nestler [a,b], Matthias Wieler [e]

[a] Institute for Applied Materials - Microstructure Modelling and Simulation (IAM-MMS), Karlsruhe Institute of Technology (KIT), Kaiserstrasse 12, 76131 Karlsruhe, Germany
[b] Institute of Digital Materials Science (IDM), Karlsruhe University of Applied Sciences, Moltkestrasse 30, 76133 Karlsruhe, Germany
[c] Institute for Applied Materials - Electrochemical Technologies (IAM-ET), Karlsruhe Institute of Technology (KIT), Kaiserstrasse 12, 76131 Karlsruhe, Germany
[d] Laboratory for Electron Microscopy (LEM), Karlsruhe Institute of Technology (KIT), Kaiserstrasse 12, 76131 Karlsruhe, Germany
[e] Computational Materials Engineering (CR/ATC1), Robert Bosch GmbH, Robert-Bosch-Campus 1, 71272 Renningen, Germany

HIGHLIGHTS

- Time-resolved multiphase-field modeling of nickel-coarsening in Ni-YSZ SOFC anode.
- Incorporation of real FIB-SEM reconstructed microstructure.
- Microstructure-property linkage by transmission-line model (TLM).
- Results reveal sensitivity of polarization resistance on wetting condition.

ARTICLE INFO

Keywords:
Solid-oxide Fuel Cells
Phase-field Modeling
Coarsening
Wetting
Diffusion
Degradation

ABSTRACT

FIB-SEM measurements of as-processed Ni-YSZ solid oxide fuel cell (SOFC) anodes are conducted. Based on the reconstructed volume as initial condition, multiphase-field simulations of nickel coarsening are performed to investigate the microstructure under operating conditions. The effect of the wettability of nickel on YSZ is discussed to span a possible range of different operating conditions. Effective properties including nickel particle size distributions, mean particle diameters, tortuosities and triple-phase boundary lengths (TPBL) serve as quantitative indicators for possible degradation and failure. The resulting data is used in a transmission-line model (TLM) to estimate anode performance and long-term stability. Generally, the simulations show that Ni coarsening at 750 °C takes place mainly in the first 100 hours. It is found that nickel coarsening is enhanced when nickel shows dewetting on YSZ. Among other findings, the TPBL decreases significantly during the simulations for all parameter sets and is insusceptible to variations in wetting angle. The TLM considers the reduction of TPBL as the main factor for degradation. Loss of nickel connectivity can lead to a further significant drop in anode performance occurring predominantly for low wettability of nickel on YSZ.

1. Introduction

Current efforts towards a sustainable future rely on an efficient and cost effective utilization of energy sources. In this regard, fuel cell technology constitutes a promising candidate to minimize carbon emissions due to its capability of efficiently converting chemical to electrical energy. Among the different types of fuel cells, solid oxide fuel cells (SOFCs) can reach the highest level of efficiency [1]. Nev ertheless, advanced materials are required to withstand the typical operating conditions at elevated temperatures of more than 700 °C. Challenges associated with the application of SOFCs include the long term degradation of the functional materials, which is due to a change in microstructural properties with time. One of the contributions to the loss of performance is attributed to the SOFC anode functional layer (AFL) in which the fuel gas reaction takes place. Inside the AFL the major contribution to the microstructural degradation is caused by nickel coarsening [2]. A detailed understanding of the underlying

* Corresponding author.
E-mail address: paul.hoffrogge@kit.edu (P.W. Hoffrogge).

mechanisms is required to deduce guidelines for the design of the anode material, which is the main motivation for our current manuscript.

The phase field technique has been employed in the context of SOFC anodes by several authors [3 16]. The studied microstructures are either artificially generated (randomly disordered [4,8], randomly closed packed [5,6], equiaxed [10] or artificially sintered [15]) or reconstructed by FIB SEM microscopy [3,7,9,11,13,14]. A recent work combined the multiphase field method and ex situ ptychographic nano tomography for the modeling of nickel coarsening in Ni YSZ elec trodes [16]. The first work by Chen et al. [3] already utilized FIB SEM reconstructed microstructures but of a limited size of less than $3.5^3\ \mu m^3$ and studied the effect of wettability on the microstructural evolution, which was also discussed in later works by Li et al. [4] and Jiao and Shikazono [11].

The mass transfer mechanisms considered vary from predominant surface (Ni Pore) diffusion [3,5], a combination of interfacial diffusion along the various phase boundaries [6], grain boundary diffusion [7,9], pure bulk diffusion [4,10,16] and a combination thereof [11,14,15]. Lei et al. [13] focused on the influence of fuel supply by considering gas diffusion of Nickel hydroxide at very high temperatures above 800 °C using a KKS type model [17]. Xiang et al. [14] studied the influence of sintering conditions and a variation in the volume fractions on the long term stability of numerous samples, each of size $10^3\ \mu m^3$. Wang et al. [15] proposed a numerical model to relate the observed microstructural changes from phase field modeling to a change in anode performance.

Inside the above works, the ceramic YSZ phase is usually considered as fully or nearly time invariant. Only in [3,10] a comparison between an evolving and non evolving YSZ phase was conducted, while the static YSZ treatment was held to be more realistic in both works independently. This is in line with experimental evidence based on a one year test of a Ni YSZ electrode [18], where only negligible changes in the particle size distribution of YSZ were observed as well as investigations after 1300 h of operation at different operation conditions revealing no change in YSZ volume fraction and tortuosity [19].

Regarding the type of phase field models in use, Chen et al. [3] utilized a multiphase Cahn Hilliard model first developed in [20]. Most of the other works [4,7,9 11,14,15] can be traced back to a work of Chen and Fan [21], which comprises of a combination of Allen Cahn and Cahn Hilliard models [22,23]. A different but related model is employed in [5,6] based on a work of Wang [24]. Among the second group of models, Lei et al. [10] modified the model [21] towards an im proved tunability of the interfacial energies, which was also later used in [15] and helps maintaining realistic wetting conditions. This model modification also achieves similar interfacial thicknesses among the different types of grain and phase boundaries. In this regard, our herein utilized model has a few notable advantages, which was analyzed and discussed in detail in our recent work [25]. The current model allows an independent control of interfacial energies for each binary interface, concomitantly maintaining equal and finite interfacial thicknesses and reproduces interfacial diffusion in a quantitative manner. This allows to accurately incorporate measured surface diffusivities and wetting angles in a straightforward manner.

Apart from the phase field model details, in the current manuscript, we aim at correlating the microstructural changes with the evolution of the performance of the anode by means of a transmission line model (TLM). This approach is common to model the electrochemi cal behavior of porous composite electrodes (e.g. Ni GDC infiltrated cermet anodes [26], LSM YSZ cathodes [27,28] or Ni ScYSZ cermet anodes [29]) and was successfully implemented by Dierickx et al. [30] for Ni YSZ anodes. While some authors moved towards similar directions e.g. through an integrated modeling approach in [5] or a so called *electrode numerical model* in [15], no work among the phase field simulations so far addresses a combination of using realistic exper imentally reconstructed microstructures and correlating the merely microstructural properties to performance. As has been shown recently by Ouyang et al. [31, Table 2], the wetting angle of nickel on YSZ can vary as a function of operating conditions. Therefore, the influence of a change in wetting angle is discussed in the current manuscript. Another important factor which in contrast to wetting angle can be controlled during manufacturing is the nickel content, which we will discuss as an additional degree of freedom in a separate second part of the work.

2. Methods

2.1. SOFC fabrication and operation

The investigated SOFC samples consist of a silicate support, a LSM YSZ cathode, YSZ electrolyte and a Ni YSZ anode (more details can be found in [32]). The functional layers were applied by screen printing and then laminated onto the substrate. The SOFC sample was co fired at a temperature between 1100 °C and 1300 °C and consecutively reduced at $T = 850\,°C$ for four hours.

2.2. FIB SEM measurement

The 3D microstructure of the Ni YSZ anode was analyzed by se quential scanning electron microscope (SEM) imaging and focused ion beam (FIB) milling. Volumes with an edge length in the range of 10 to 100 micrometer at a resolution as good as 10 nm can be reliably detected [33,34]. The specimens were infiltrated with an epoxy resin (EpoFix, Struers GmbH, Willich, Germany) under vacuum conditions to infiltrate the pores. This allows SEM examination without topographic contrast. After polishing with SiC paper, the samples were mounted on a sample holder. Charging is reduced by using an electrically conduc tive silver adhesive and by sputtering a platinum coating. Datasets for FIB/SEM tomography were obtained with a Thermo Scientific™ Helios G4 FX DualBeam™ (Thermo Fisher Scientific, Waltham, Massachusetts, USA) microscope. A good material contrast between nickel and YSZ was obtained with the through the lens secondary electron detector (TLD) in charge neutralization mode at an electron energy of 3 keV and a beam current of 0.8 nA (cf. [32,34]). During FIB/SEM tomography the Ga^+ ion beam current was set to 2.4 nA at 30 keV.

The image stack was aligned using ImageJ Fiji [35]. Gradients in image grayscale and noise were reduced by several filtering steps such as anisotropic diffusion filtering [36,37]. The filtered images were segmented using a region growing algorithm [38], which gives better results for three phase materials compared to threshold based segmentation. A volume of size $L_x \times L_y \times L_z = 15\,\mu m \times 15\,\mu m \times 9.2\,\mu m$ is reconstructed for the studies herein which is shown in Fig. 1(a). This microstructure serves as initial condition for the simulations.

2.3. Multiphase field model

2.3.1. Model equations

A multiphase field model is employed to model the coarsening of nickel. The model is derived from a grand potential functional accord ing to Choudhury and Nestler [39] and a recent extension is utilized to delineate surface self diffusion of nickel [25]. The model is formulated by means of the grand potential functional Ψ (in J), which depends on the order parameters $\boldsymbol{\phi} = \{\phi_\alpha, \phi_\beta, \dots, \phi_N\}$ (dimensionless) and the volumetric chemical potentials $\boldsymbol{\mu} = \{\mu_1, \mu_2, \dots, \mu_{K-1}\}$ (in $J\,m^{-3}$), and is written as

$$\Psi(\boldsymbol{\phi}, \boldsymbol{\nabla\phi}, \boldsymbol{\mu}) = \int_V \frac{1}{\epsilon} w(\boldsymbol{\phi}) + \epsilon a(\boldsymbol{\nabla\phi}) + \psi(\boldsymbol{\phi}, \boldsymbol{\mu})\, dV\,. \tag{1}$$

Here, $w(\boldsymbol{\phi})$ (in $J\,m^{-2}$) and $a(\boldsymbol{\nabla\phi})$ (in J/m^4) are the potential and gradient terms following the notation of [40] which are responsible for the

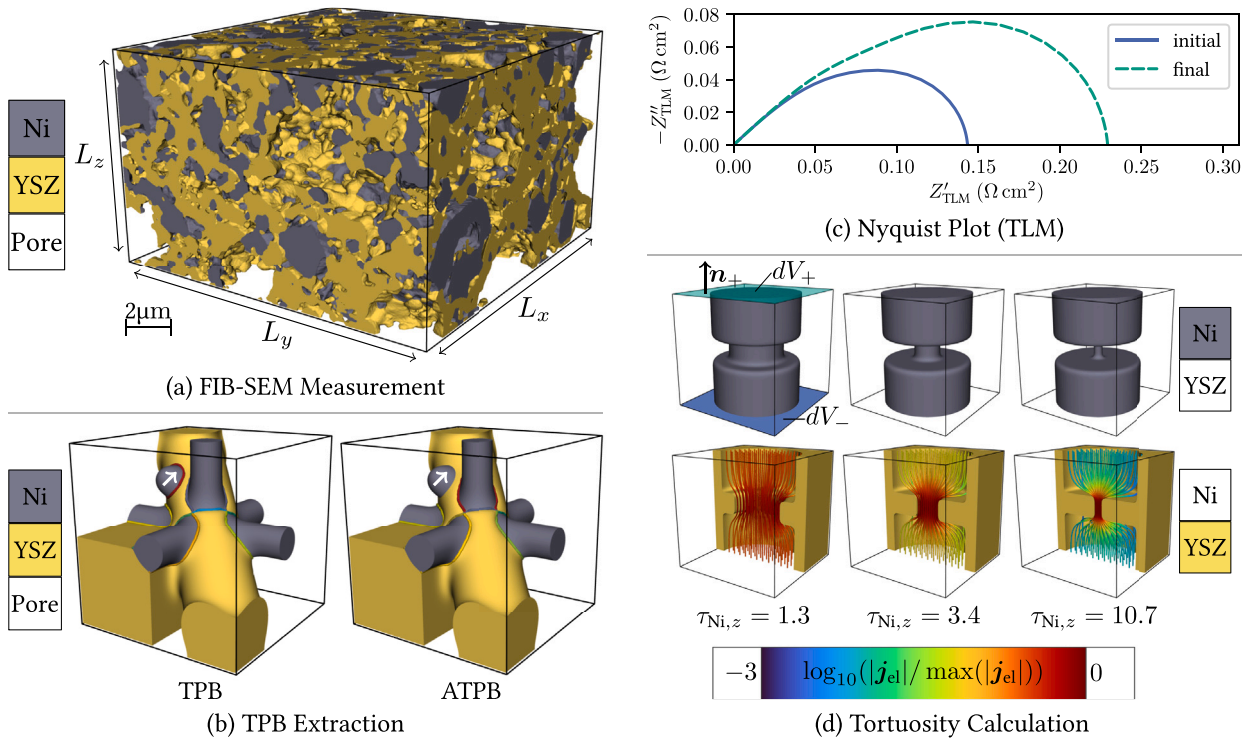

Fig. 1. Overview over the methods used in the current work. Initial FIB-SEM measured anode structure (a), total and active triple-phase boundary for an exemplary geometry with a highlighted inactive segment (b), Nyquist plot of the calculated impedance spectra (cf. Eq. (14)) exemplarily for structure $\theta = 104°$ at $t = 0\,\mathrm{h}$ and $t = 1127\,\mathrm{h}$ (c), tortuosities for cylindrical geometries with varying neck diameters and corresponding electric streamlines inside the nickel phase (d).

stabilization of the interfacial profile of finite thickness and introduce interfacial energy into the model. The parameter ϵ (a length in m) controls the thickness of the sinusoidal interface profile $\delta = \epsilon\pi^2/4$. The gradient term is chosen according to [41] as

$$a(\nabla\boldsymbol{\phi}) = -\sum_{\substack{\alpha,\beta=1\\ \alpha<\beta}}^{N,N} \gamma_{\alpha\beta}\nabla\phi_\alpha\cdot\nabla\phi_\beta \tag{2}$$

where $\gamma_{\alpha\beta}$ is the interfacial energy in $\mathrm{J\,m^{-2}}$ between phases α and β. An obstacle type potential is utilized which reads

$$w(\boldsymbol{\phi}) = \begin{cases} \frac{16}{\pi^2}\sum_{\substack{\alpha,\beta=1\\ \alpha<\beta}}^{N,N}\gamma_{\alpha\beta}\phi_\alpha\phi_\beta, & \boldsymbol{\phi}\in\mathcal{G} \\ \infty, & \boldsymbol{\phi}\notin\mathcal{G}. \end{cases} \tag{3}$$

The Gibbs simplex

$$\mathcal{G} = \left\{ \sum_{\alpha=1}^{N}\phi_\alpha = 1 : \{\phi_\alpha \geq 0,\ \forall\,\alpha\in\{1,\dots,N\}\} \right\} \tag{4}$$

guarantees that the order parameters are bound between zero and unity. The grand potential density

$$\psi(\boldsymbol{\phi},\boldsymbol{\mu}) = \sum_{\alpha=1}^{N}\psi^\alpha(\boldsymbol{\mu})h_\alpha(\boldsymbol{\phi}) \tag{5}$$

comprises of phase inherent terms

$$\psi^\alpha(\boldsymbol{\mu}) = f^\alpha(\boldsymbol{c}^\alpha(\boldsymbol{\mu})) - \sum_{i=1}^{K-1}\mu_i c_i^\alpha(\boldsymbol{\mu}), \forall\,\alpha\in\{1,\dots,N\} \tag{6}$$

and contributes bulk free energies f^α to the functional. These depend on the phase inherent compositions $\boldsymbol{c}^\alpha = \{c_1^\alpha, c_2^\alpha, \dots, c_{K-1}^\alpha\}$. The interpolation function h_α satisfies the constraint

$$\sum_{\alpha=1}^{N} h_\alpha(\boldsymbol{\phi}) = 1\,. \tag{7}$$

In the current manuscript, $h_\alpha(\boldsymbol{\phi}) = \phi_\alpha$ is chosen. A quasi equilibrium is assumed locally, such that at any position in space

$$\mu_i = \frac{\partial f^\alpha(\boldsymbol{c}^\alpha)}{\partial c_i^\alpha} = \frac{\partial f^\beta(\boldsymbol{c}^\beta)}{\partial c_i^\beta} = \dots = \frac{\partial f^N(\boldsymbol{c}^N)}{\partial c_i^N} \tag{8}$$

is satisfied for all $i\in\{1,\dots,K-1\}$.

The evolution equation of the order parameters is according to [41] written as

$$\epsilon\frac{\partial\phi_\alpha(\boldsymbol{x},t)}{\partial t} = \frac{1}{\tilde{N}}\sum_{\substack{\beta=1\\ \beta\neq\alpha}}^{N} m_{\alpha\beta}\left(\frac{\delta\Psi}{\delta\phi_\beta} - \frac{\delta\Psi}{\delta\phi_\alpha}\right) \tag{9}$$

where $\tilde{N}$ denotes the local number of phases, $m_{\alpha\beta}$ (units of $\mathrm{m^4/J/s}$) stands for the mobility of the interface between phases α and β and $\delta/(\delta\phi_\alpha)$ is the partial functional derivative with respect to ϕ_α. Nickel and YSZ are treated as pure solids of nearly fixed compositions by introducing free energies of the form $f^\alpha(c^\alpha(\boldsymbol{\mu})) = \sum_{i=1}^{K-1} f_i^\alpha(\mu_i)$, where the individual contributions are assumed as simple parabolas, i.e. $f_i^\alpha(\mu_i) = A_i(c_i^\alpha(\mu_i) - c_{i,\mathrm{eq}}^\alpha)^2$, $i\in\{\mathrm{Ni},\mathrm{YSZ}\}$. Here, the prefactor A_i represents the strength of immiscibility and is taken sufficiently high to allow for volume conservation of each of the phases. We neglect any subgrain structure, i.e. all phenomena corresponding to the existence of grain boundaries such as grain boundary migration and diffusion. The implied limitations are discussed in Section 4.1 and in part II of the work.

We model the porous Ni YSZ system by a set of two dimensionless composition variables $\boldsymbol{c} \equiv \{c_{\mathrm{Ni}}, c_{\mathrm{YSZ}}\}$ (mole fractions), i.e. $K = 3$. The composition of the porous phase is then just $c_{\mathrm{Pore}} = 1 - \sum_{i=1}^{K-1} c_i = 1 - c_{\mathrm{YSZ}} - c_{\mathrm{Ni}}$. The dimensionless composition fields $c_i = \sum_{\alpha=1}^{N} h_\alpha c_i^\alpha$ (mole fractions) are conservative and accordingly evolve as

$$\frac{\partial c_i(\boldsymbol{x},t)}{\partial t} = -\nabla\cdot\boldsymbol{j}_i, \tag{10}$$

where $\boldsymbol{j}_i$ represents the flux of the species i in units of $\mathrm{m\,s^{-1}}$. Based on Eq. (10) and the quasi equilibrium condition Eq. (8), the evolution of

the ith chemical potential is written in Einstein notation as

$$\frac{\partial \mu_i(\boldsymbol{x},t)}{\partial t} = \left[\sum_{\alpha=1}^{N} h_\alpha(\boldsymbol{\phi}) \frac{\partial c_j^\alpha(\boldsymbol{\mu})}{\partial \mu_i}\right]^{-1} \left[\frac{\partial c_j(\boldsymbol{x},t)}{\partial t} - \sum_{\alpha=1}^{N} c_j^\alpha(\boldsymbol{\mu}) \frac{\partial h_\alpha(\boldsymbol{\phi}(\boldsymbol{x},t))}{\partial t}\right]. \tag{11}$$

The mobilities for the diffusion of the species, which govern the evo lution of the system are so chosen to neglect diffusion of the ceramic phase $\boldsymbol{j}_{\mathrm{YSZ}} = \boldsymbol{0}$ while we assume surface diffusion to be the dominant mass transfer mechanism for nickel in the typical operating tempera ture range of the SOFC. Therefore, the flux density of nickel is written as

$$\boldsymbol{j}_{\mathrm{Ni}} = -\frac{32}{\pi^2 \epsilon} M_{\mathrm{Ni}}^{\mathrm{NiPore}} \phi_{\mathrm{Ni}} \phi_{\mathrm{Pore}} \boldsymbol{\nabla} \mu_{\mathrm{Ni}}\,. \tag{12}$$

The mobility $M_{\mathrm{Ni}}^{\mathrm{NiPore}}$ (units of $\mathrm{m}^6/\mathrm{J/s}$) controls the diffusion of nickel along the tangential direction of the free nickel surface and is related to the surface self diffusivity D_s by an Einstein like relation (cf. [25, Eq. (99)]), that reads

$$M_{\mathrm{Ni}}^{\mathrm{NiPore}} = \frac{D_s \delta_s V_m (\Delta c_{\mathrm{Ni},eq}^{\mathrm{Ni-Pore}})^2}{RT}\,. \tag{13}$$

Here δ_s is the atomistic thickness of the nickel surface (in the order of 0.1 nm), V_m the molar volume of nickel, R and T the ideal gas constant and temperature, respectively. For instance, Maiya and Blakely [42] assumed $\delta_s = a_0/\sqrt{h^2+k^2+l^2}$, with the lattice parameter for nickel $a_0 = 0.352\,\mathrm{nm}$ and Miller indices $\{hkl\}$, which results in $\delta_s = 0.352\,\mathrm{nm}$ and $\delta_s = 0.249\,\mathrm{nm}$ for the $\{100\}$ and $\{110\}$ surfaces, respectively. As the value of the intrinsic interface diffusivity D_s alone is unimportant and only the product with the interface thickness enters the equation above, we denote the quantity $D_{s,\mathrm{ex}} \equiv D_s \delta_s$ (which has dimensions $\mathrm{m}^3\,\mathrm{s}^{-1}$) as the excess surface diffusivity of nickel, which removes the need to assume a somewhat arbitrary interface thickness δ_s. The model specific composition difference $\Delta c_{\mathrm{Ni},eq}^{\mathrm{Ni-Pore}}$ is defined as $\Delta c_{\mathrm{Ni},eq}^{\mathrm{Ni-Pore}} \equiv c_{\mathrm{Ni,eq}}^{\mathrm{Ni}} - c_{\mathrm{Pore,eq}}^{\mathrm{Ni}} = 0.8$.

During the simulation, the domain boundaries are treated as isolat ing (i.e. $\boldsymbol{j}_i \cdot \boldsymbol{n} = 0 \,\forall\, i,\ \boldsymbol{x} \in dV$) and perpendicular contact is assumed for each of the particles ($\boldsymbol{\nabla}\phi_\alpha \cdot \boldsymbol{n} = 0 \,\forall\, \alpha,\ \boldsymbol{x} \in dV$).

For the current document, a SIMD vectorized solver is utilized, the implementation is detailed in [43, Sec. 4.2]. For the validation of the model, the interested reader is referred to [25]. In the current setup, which relies on $\boldsymbol{j}_{\mathrm{YSZ}} = \boldsymbol{0}$, the YSZ composition remains fixed, while the order parameter ϕ_{YSZ} might still evolve according to its evolution equation. This helps avoiding any unwanted pinning effects and allows treating the YSZ phase without a separate diffuse wetting boundary condtion, as e.g. presented in [44]. Nevertheless, an initialization step is required to maintain a sufficiently diffuse and sinusoidal interface profile at the YSZ surface, which is performed herein analogously to [45] by removing the curvature term in the evolution equation and in the absence of any chemical driving force. The initialization step is terminated when the interface profile shows only negligible changes. Thereafter, no special treatment is required. To see that the current approach is capable of reproducing Young's law on a substrate, a validation study is presented in Appendix.

2.3.2. Parameterization of the model

The parameterization of the model is presented in Table 1. Note that, for the sake of convenience, the model parameters are specified with respect to a model specific unit system. Accordingly, u_l, u_E and u_t denote length, energy and time units of the model, respectively. The length unit u_l is affixed by taking into account the resolution of the initial microstructure (Δx), whereas energy and time units can be related by including interfacial energy γ_{NiPore}, diffusivity D_s and temperature T (see Eq. (13)), respectively.

To affix $M_{\mathrm{Ni}}^{\mathrm{NiPore}}$, it is assumed, following the results presented in [46], that diffusion along the slow $\{100\}$ surface orientation is the limiting factor. Therefore, the average of the four datapoints in [46, Fig. 8] near $\{100\}$ yield an excess surface diffusivity of $D_{s,\mathrm{ex}} = 3.75 \times 10^{-22}\,\mathrm{m}^3\,\mathrm{s}^{-1}$ at $T = 750\,^\circ\mathrm{C}$. The surface energy of nickel γ_{NiPore} is chosen according to Haremski et al. [47, Section 4.4] at 750 °C. For a variation in the wetting angle θ (cf. Appendix), only the difference of γ_{NiYSZ} and $\gamma_{\mathrm{PoreYSZ}}$ is relevant. Therefore, without loss of generality, $\gamma_{\mathrm{PoreYSZ}}$ was assigned identical value as γ_{NiPore} and the wetting angle is controlled by modifying γ_{NiYSZ}.

The selection strategy for the considered wetting angles is as fol lows. Firstly, the difference in wetting angles between the simulations should be significant to permit clear trends in the simulation results such that the observed differences can reasonably be attributed to the variations in wetting angle. Secondly, the full range of possible wetting conditions is covered, including wetting ($\theta < 90°$) and dewetting condi tions ($\theta > 90°$), as well as the intermediate case $\theta = 90°$. The maximum angle studied is $\theta = 104°$ which is within the range of observed wetting angles of roughly 100 to 160° in [31] and hence is considered the most realistic scenario. While the studied angles smaller than 100° may not be achievable in experiment, we think that the current study provides interesting evidence whether anode sided degradation can be minimized by means of an improved wetting. Studying the practical feasibility of such steps towards a better wetting of nickel on YSZ is not the scope of the current manuscript.

The mobilities $m_{\alpha\beta}$ are so chosen to be small enough to operate in the surface diffusion controlled limit (cf. [25, Eq. (99) ff.]) and thus are not the governing rate constants. The minimas of the parabolic free energy are chosen such that $c_{i,\mathrm{eq}}^\alpha$ is small if the corresponding phase α does not correspond to the component i, and large otherwise. The re spective values 0.1 and 0.9 are not entirely meaningful, the importance lies in keeping sufficiently distinct values in order to allow a separation into e.g. Ni rich and poor phases. Lowering the difference between the two values requires higher values of A_i in order to maintain the same level of volume preservation, and vice versa.

2.4. Transmission line model

Microstructure properties can be correlated to electrochemical be havior using a transmission line model (TLM) approach as illustrated in [30]. In nickel YSZ fuel electrodes the electrochemical oxidation of hydrogen takes place at the TPB where all transport paths converge: (i) electronic conduction in the nickel phase, (ii) ionic conduction in the YSZ phase and (iii) gas diffusion in the pores. Gas diffusion losses as well as losses of the electronic path through the nickel are neglected due to the small layer thickness of 10 µm to 15 µm and the high conductivity of nickel compared to YSZ ($\sigma_{\mathrm{el,Ni}} > 10^5 \times \sigma_{\mathrm{ion,YSZ}}$). This leads to a simplified TLM which considers microstrucure based ionic losses through the YSZ within the fuel electrode as well as a charge transfer resistance at the TPB

$$Z_{\mathrm{TLM}}(\omega) = \sqrt{\zeta(\omega)\,\chi_1}\,\coth\left(l\sqrt{\frac{\chi_1}{\zeta(\omega)}}\right) \tag{14}$$

with charge transfer reaction ζ, layer thickness l and ionic transport resistance

$$\chi_1 = \frac{1}{A_{\mathrm{act}}\,\sigma_{\mathrm{ion,eff}}} \tag{15}$$

based on active electrode area $A_{\mathrm{act}} = 1\,\mathrm{cm}^2$ and effective ionic conduc tivity

$$\sigma_{\mathrm{ion,eff}} = \frac{X_{\mathrm{YSZ}}}{\tau_{\mathrm{YSZ}}} \cdot \sigma_{\mathrm{ion}} \tag{16}$$

considering the three dimensional microstructure of the ionic phase expressed in YSZ material fraction X_{YSZ} and tortuosity τ_{YSZ}. Due to an initial YSZ phase transformation from cubic to tetragonal initiated during reduction, the ionic conductivity at an operation temperature of 750 °C is $\sigma_{\mathrm{ion}} = 2.84\,\mathrm{S\,m^{-1}}$ [48,49]. The charge transfer reaction ζ can be modeled with an RQ element with time constant of the

Table 1
Parameter set for the modeling of Ni-YSZ anode. The model units are expressed as $u_l = 25\,\text{nm}$, $u_E = 1.43 \times 10^{-15}\,\text{J}$, $u_t = 9.2 \times 10^{-2}\,\text{s}$.

Parameter	Symbol	Value (model units)	Value (physical units)
Diffusion coefficient Ni-surface	$M_{\text{Ni}}^{\text{NiPore}}$	0.1 $u_l^6/(u_E u_t)$	$1.86 \times 10^{-31}\,\text{m}^6/\text{J/s}$
Interfacial energy Ni-Pore	γ_{NiPore}	1.0 u_E/u_l^2	$2.29\,\text{J m}^{-2}$
Interfacial energy Ni-YSZ	γ_{NiYSZ}	0.75 … 1.25 u_E/u_l^2	1.71 … 2.87 J m^{-2}
Interfacial energy Pore-YSZ	γ_{PoreYSZ}	1.0 u_E/u_l^2	$2.29\,\text{J m}^{-2}$
Interface mobility Ni-Pore	m_{NiPore}	0.1 $u_l^4/(u_E u_t)$	$2.97 \times 10^{-16}\,\text{m}^4/\text{J/s}$
Interface mobility Ni-YSZ	m_{NiYSZ}	1.0 $u_l^4/(u_E u_t)$	$2.97 \times 10^{-15}\,\text{m}^4/\text{J/s}$
Interface mobility Pore-YSZ	m_{PoreYSZ}	1.0 $u_l^4/(u_E u_t)$	$2.97 \times 10^{-15}\,\text{m}^4/\text{J/s}$
Interface width parameter	ϵ	2.0 u_l	50 nm
Voxel-size	$\Delta x = \Delta y = \Delta z$	1.0 u_l	25 nm
Thermodynamic prefactor Nickel	A_{Ni}	5 u_E/u_l^3	$4.58 \times 10^8\,\text{J/m}^3$
Thermodynamic prefactor YSZ	A_{YSZ}	50 u_E/u_l^3	$4.58 \times 10^9\,\text{J/m}^3$
Equil.-comp. Ni-Ni	$c_{\text{Ni,eq}}^{\text{Ni}}$	0.9	90 mol%
Equil.-comp. Ni-YSZ	$c_{\text{Ni,eq}}^{\text{YSZ}}$	0.1	10 mol%
Equil.-comp. Ni-Pore	$c_{\text{Ni,eq}}^{\text{Pore}}$	0.1	10 mol%
Equil.-comp. YSZ-Ni	$c_{\text{YSZ,eq}}^{\text{Ni}}$	0.1	10 mol%
Equil.-comp. YSZ-YSZ	$c_{\text{YSZ,eq}}^{\text{YSZ}}$	0.9	90 mol%
Equil.-comp. YSZ-Pore	$c_{\text{YSZ,eq}}^{\text{Pore}}$	0.1	10 mol%

charge transfer τ_{CT}, charge transfer resistance R_{CT}, imaginary number j, angular frequency ω and homogeneity exponent n ($0 \leq n \leq 1$):

$$\zeta(\omega) = \frac{R_{\text{CT}}}{1 + (j\omega\tau_{\text{CT}})^n}\,. \tag{17}$$

The charge transfer resistance R_{CT} is influenced by the active triple phase boundary length, l_{ATPB}, A_{act} and the line specific resistance of the charge transfer LSR_{CT} which was calculated as $158.14\,\Omega\,\text{m}$ (5.5% H_2O in H_2, $T = 750\,^\circ\text{C}$) [50,51]:

$$R_{\text{CT}} = \frac{\text{LSR}_{\text{CT}}}{l_{\text{ATPB}}\,A_{\text{act}}} \tag{18}$$

The time constant of the charge transfer is given by

$$\tau_{\text{CT}} = R_{\text{CT}} C \tag{19}$$

with the capacitance

$$C = A_{\text{act}}\left(\text{LSC}_{\text{CT}}\,l_{\text{ATPB}} + \text{ASC}_{\text{DL}}\,A_{\text{Ni-YSZ}}\right) \tag{20}$$

including line specific capacitance of the charge transfer LSC_{CT} and area specific capacitance of the double layer ASC_{DL} according to [51]. The contact area between nickel and YSZ, $A_{\text{Ni-YSZ}}$, was initially cal culated from reconstructed electrode volume obtained by FIB SEM. Time dependent values are simulated in the multiphase field model.

The parameters needed to calculate the complex impedance spec trum of the Ni YSZ anode are summarized in Table 2. The Nyquist dia gram (cf. Fig. 1(c)) shows the negative imaginary part of the impedance spectrum plotted against its real part. Here $Z'_{\text{TLM}} \equiv \text{Re}(Z_{\text{TLM}})\,A_{\text{act}}$ and $Z''_{\text{TLM}} \equiv \text{Im}(Z_{\text{TLM}})\,A_{\text{act}}$ denote the specific real and imaginary part of the anode impedance, respectively.

The polarization resistance, R_{pol}, which represents the losses in the Ni YSZ anode can be determined by calculating the x axis interval between the low and high frequency intersections of the impedance curve with the real axis, i.e.

$$R_{\text{pol}} = Z'_{\text{TLM}}(0) - \lim_{\omega\to\infty} Z'_{\text{TLM}}(\omega)\,. \tag{21}$$

The example in Fig. 1(c) shows that the aging of the anode during operation leads to an increase in polarization resistance of 65% from $0.14\,\Omega\,\text{cm}^2$ to $0.23\,\Omega\,\text{cm}^2$.

2.5. Effective microstructural parameters

2.5.1. Tortuosity

The tortuosity τ_α of a phase α is a dimensionless parameter related to its geometry and gives a measure for the specific resistance under electrostatic conditions [52]. It is inversely related to the effective conductivity of the phase (see Eq. (16)). The electric potential P (units of V) satisfies the Laplace equation $\nabla^2 P = 0$ under electrostatics and for an isotropic electric conductivity σ (units of S m^{-1}). Therefore, the problem reduces to solve for the Laplace equation under certain boundary conditions. To drive electron conduction, Dirichlet boundary conditions $P(\boldsymbol{x} \in dV_-) = 0\,\text{V}$ and $P(\boldsymbol{x} \in dV_+) = 1\,\text{V}$ are applied at two opposing flat boundaries $dV_\pm$ with outward normals $\boldsymbol{n}_\pm = \pm\boldsymbol{n}_+ = \pm\boldsymbol{e}_x$. Here $\boldsymbol{e}_x$ is the Cartesian base vector in one of the sample directions, such that the location of the boundaries can be written as $\boldsymbol{x}\cdot\boldsymbol{e}_x = 0\;\forall\boldsymbol{x} \in dV_-$ and $\boldsymbol{x}\cdot\boldsymbol{e}_x = L_x\;\forall\boldsymbol{x} \in dV_+$, where L_x is the size of the sample in direction x. Additionally, no flux boundary conditions are imposed on the current density $\boldsymbol{j}_{\text{el}} \equiv -\sigma\boldsymbol{\nabla}P$. Therefore, $\boldsymbol{j}_{\text{el}}\cdot\boldsymbol{n}_\alpha = 0\;\forall\boldsymbol{x} \in dV_\alpha \setminus (dV_- \cup dV_+)$ where dV_α denotes the surface bounding the α phase with normal $\boldsymbol{n}_\alpha$, which corresponds to treating the interfaces and non Dirichlet boundaries as isolating. Finally, the total magnitude of the electric current is computed as the surface integral, $I = \sigma\int_{dV_+}\boldsymbol{\nabla}P\cdot\boldsymbol{n}_+ dA$, or alternatively due to the divergence theorem $I = \sigma\int_{dV_-}\boldsymbol{\nabla}P\cdot\boldsymbol{n}_+ dA$. The tortuosity $\tau_{\alpha,x}$ of a phase α, measured in direction x, is defined as the ratio of a hypothetical ideal current $I_{\text{ideal},\alpha} = (\sigma V X_\alpha \Delta P)/L_x^2$ and the actual current, i.e.

$$\tau_{\alpha,x} \equiv \frac{I_{\text{ideal},\alpha}}{I} = \frac{\sigma V X_\alpha \Delta P}{L_x^2\,I}\,. \tag{22}$$

The incoporation of the ideal current ensures that the tortuosity is scale invariant. Here, V is the total volume, $\Delta P \equiv P(\boldsymbol{x} \in dV_+) - P(\boldsymbol{x} \in dV_-) = 1\,\text{V}$ is the imposed voltage difference, X_α is the total volume fraction of phase α. The value of the electrical conductivity σ enters linearly both in the numerator as well as in the denominator of Eq. (22) and is hence unimportant. Thus, τ_α is a purely geometrical property. The ideal current can be understood to correspond to a structure with identical volume fraction X_α but only transport pathways parallel to $\boldsymbol{n}_+$. Since the ideal current is the maximum possible, one gets $\tau_\alpha \geq 1$ for arbitrary microstructures. The resulting tortuosities for simple cylin drical geometries with varying neck diameter are shown in Fig. 1(d). Here, increasing tortuosity values reflect that the electron transport becomes less effective as the neck diameter decreases. The magnitude of the current density $|\boldsymbol{j}_{\text{el}}|$ and streamlines (lines parallel to $\boldsymbol{\nabla}P$), shown in the bottom row of Fig. 1(d), can be used to highlight locations of bottlenecks along the tortuos electron pathways in the microstructure. In the current work, mean tortuosities

$$\tau_\alpha \equiv \frac{1}{3}\left(\tau_{\alpha,x} + \tau_{\alpha,y} + \tau_{\alpha,z}\right) \tag{23}$$

Table 2
Parameter set used to calculate the impedance Z_{TLM} (cf. Eq. (14)) of the Ni-YSZ anode via transmission-line model (temperature: $T = 750\,°C$, fuel gas: 5.5% H_2O in H_2).

Parameter	Symbol	Value	Reference
Line specific resistance of charge transfer	LSR_{ct}	$158.14\,\Omega\,m$	[50,51]
Line specific capacitance of the charge transfer	LSC_{CT}	$5.99 \times 10^{-6}\,F\,m^{-1}$	[51]
Area specific capacitance of the double layer	ASC_{DL}	$2.53\,F\,m^{-2}$	[51]
Ionic conductivity YSZ	σ_{ion}	$2.84\,S\,m^{-1}$	[48,49]
Active electrode area	A_{act}	$1\,cm^2$	–
Layer thickness	l	$10\,\mu m$	–
YSZ material fraction	X_{YSZ}	0.323	–
YSZ tortuosity	τ_{YSZ}	2.7	–
Triple-phase boundary length	l_{ATPB}		cf. Fig. 5

and corresponding standard deviations

$$\Delta\tau_\alpha \equiv \sqrt{\frac{1}{3}\sum_{i\in\{x,y,z\}}\left(\tau_{\alpha,i}-\tau_\alpha\right)^2} \tag{24}$$

are utilized for the anode structures to quantify the effect of structural anisotropy.

2.5.2. Triple phase boundary length

The triple phase boundary is calculated by means of a skeletonization algorithm [53]. In a first step, the set of voxels simultaneously belonging to the vicinity of all three phases are marked. In the next step, the thickness of these several voxel thick tubes is reduced by skeletonization to a thickness of a single voxel from which an undirected graph is constructed by connecting neighboring voxels. In a last step, the resulting network is smoothed to minimize the effect of the discretization. This method, which readily provides connectivity information, allows to highlight individual segments of the TPB with different colors, as in Fig. 1(b). In the current work, TPB segments are considered as inactive once they lack a connection to one of the domain boundaries through at least one of the three phases. The TPB without the inactive segments is called active TPB (ATPB).

2.5.3. Continuous particle size distribution

To quantify the particle size during the coarsening of nickel, continuous particle size distributions according to Münch and Holzer [54] are utilized. This method is particularly useful for porous networks, as it elegantly avoids an artificial segmentation into particles. The method has been successfully applied to experimental measurements of SOFC anode materials [55]. The continuous particle size distribution corresponds to the relative volume of a certain phase that can be filled with overlapping spheres of a certain diameter. As the diameter increases, this relative amount decreases since sharp features in the microstructure cannot be swept with large spheres. The continuous particle distribution goes from unity to zero in a monotonous fashion and hence corresponds to a complementary cumulative distribution. The mean particle size d_{50} is obtained from the point where this distribution assumes a value of 0.5, and thus may be more strictly interpreted as the median particle size. In addition to the cumulative PSD, we will frequently show plots of the PSD density, which is derived as the negative slope of the continuous PSD. In the current work the density is calculated from the cumulative distribution by finite differences which leads to a histogram dataset.

2.5.4. Specific areas

Specific areas A_α are calculated for each phase by integrating the magnitude of its order parameter, i.e.

$$A_\alpha = \frac{1}{V}\int_V |\nabla\phi_\alpha| dV\,. \tag{25}$$

Therefrom, the areas $A_{\alpha\text{-}\beta}$ of the individual interfaces between phases α and β are derived by solving the following system of linear equations

$$A_{Ni} = A_{Ni\text{-}Pore} + A_{Ni\text{-}YSZ} \tag{26}$$

$$A_{YSZ} = A_{Ni\text{-}YSZ} + A_{Pore\text{-}YSZ} \tag{27}$$

$$A_{Pore} = A_{Ni\text{-}Pore} + A_{Pore\text{-}YSZ}\,. \tag{28}$$

3. Simulation results

3.1. Microstructural properties

3.1.1. Evolution at $\theta = 104°$

The evolution of the FIB SEM reconstructed anode microstructure is shown exemplarily for a wetting angle of $\theta = 104°$ in Fig. 2. It can be seen that the nickel particles become smooth and partially agglomerate during the simulation. On the contrary, during the whole procedure, the YSZ network remains invariant, as desired. In some areas, exemplarily highlighted by a black frame in Fig. 2, further nickel growth is prohibited by the dense YSZ network which encapsulates some of the fine metallic particles. At late times, the growth of large particles inside large cavities is dominant (highlighted by a red frame inside Fig. 2), while most of the small particles have already reached an almost temporally invariant shape (e.g. black frame).

To quantitatively investigate the nickel coarsening, continuous particle size distributions are shown in Fig. 3 for different times. Initially, the microstructure comprises of particles ranging roughly from $0.4\,\mu m$ to $1.2\,\mu m$ in diameter, while the cumulative distribution shows an almost symmetrical sigmoid shape. In the course of the evolution, the distribution shifts towards larger particle sizes. At later times, the shift of the distribution increases much slowly with time, while the tail of the distribution develops in a more pronounced fashion, which corresponds to the growth of large particles. Consequently, the final distribution after a total of 1127 h, is relatively asymmetric in relation to the initial one. From the distributions, the evolution of the mean particle diameter d_{50} is derived and shown in Fig. 4. Here, it is observed that the coarsening of nickel, starting from a mean diameter of about $d_{50} = 0.77\,\mu m$ predominantly occurs in the early time and considerably slows down at a later time, where a diameter of $d_{50} = 0.98\,\mu m$ is approached in the final state. The accelerated growth in early time is generally consistent with experimental findings (cf. an overview in [55, Fig. 16] containing data from [56–58]).

3.1.2. Influence of the wetting angle

To investigate the influence of the wetting angle, two additional simulations with a different choice of the interfacial energies $\gamma_{\alpha\beta}$ have been performed. The characteristic microstructural properties of the three simulations at varying wetting angles are summarized in Table 3 for annealing times of 100 h and 1000 h.

PSD densities in the final state are shown in Fig. 5(a) where it is found that larger wetting angles favor large ($> 1.5\,\mu m$) nickel particles in expense of small ($< 1\,\mu m$) particles. Moreover, the smaller the wetting angle, the larger the skewness of the respective final distributions. As shown in Fig. 5(b), it is observed that the evolution of the mean particle diameter is strongly influenced by the wetting angle, while smaller wetting angles lead to significantly reduced increase in particle size. However, all three cases show a similar qualitative behavior of coarsening, i.e. an accelerated growth at early time. Pronounced quantitative differences can be observed between the three cases, which correspond to final particle diameters of $0.98\,\mu m$, $0.89\,\mu m$ and $0.79\,\mu m$ for decreasing wetting angles, respectively. This shows, that the wetting

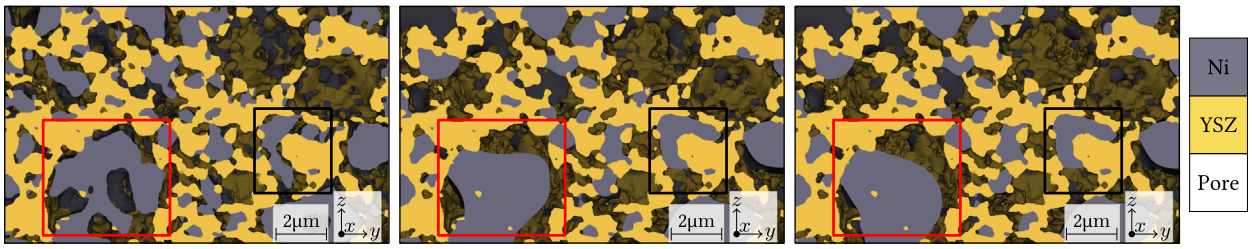

Fig. 2. Two-dimensional cross-section view of the three-dimensional microstructure ($\theta = 104°$) as it evolves during the simulation. Red and black frames highlight the evolution of a large particle and fine nickel arrangements, respectively. Shaded regions illustrate nickel and YSZ particles out of the cross-sectional plane while the pore phase is rendered transparently. The transport direction corresponds to the z-direction. (For interpretation of the references to color in this figure legend, the reader is referred to the web version of this article.)

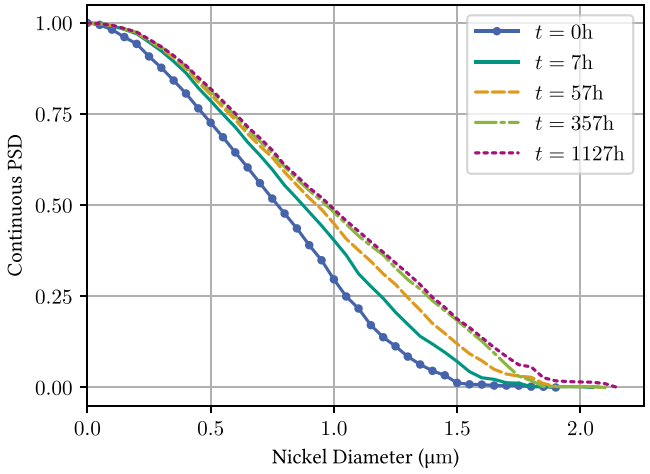

Fig. 3. Continuous particle size distribution of the nickel phase at different times during simulated annealing at 750 °C.

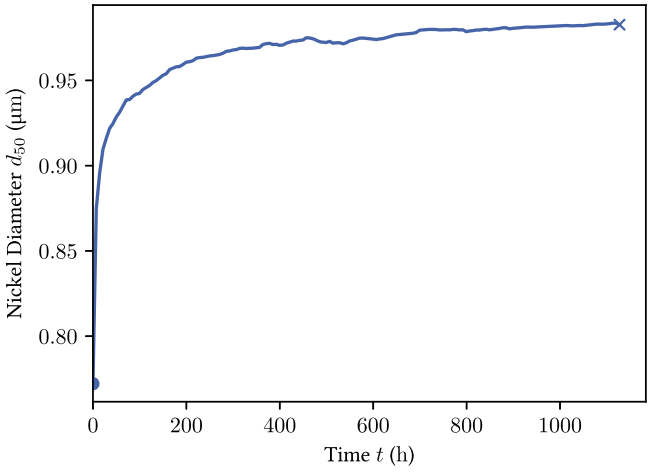

Fig. 4. Nickel particle diameter in the course of the MPF simulation.

angle sensitively controls the material behavior and that a wetting angle of 76° is sufficient to nearly suppress net nickel growth.

Fig. 5(c) shows the evolution of the nickel tortuosity for varying wetting angles. One might argue that the electron transport is not the reaction rate limiting process and hence unimportant, but the large tortuosities indicate a high likelihood to face the formation of nickel islands and hence can be considered as a stability indicator for the operation of the anode material. It is observed that for the case of high

Table 3
Characteristic microstructural properties of three simulations with varying wetting angles.

θ (°)	t (h)	τ_{Ni} (–)	τ_{Pore} (–)	τ_{YSZ} (–)	d_{50} (µm)	l_{TPB}/l_{ATPB} (µm^{-2})	$A_{Ni\ Pore}$ (µm^{-1})	$A_{Ni\ YSZ}$ (µm^{-1})	$A_{Pore\ YSZ}$ (µm^{-1})
76	0	21	3.6	2.7	0.77	3.6/2.4	0.72	0.72	1.3
76	100	12	4.0	2.7	0.78	2.2/1.6	0.39	0.93	1.1
76	1000	11	4.3	2.7	0.79	1.9/1.4	0.33	0.96	1.1
90	0	21	3.6	2.7	0.77	3.6/2.4	0.72	0.72	1.3
90	100	21	3.6	2.7	0.87	2.2/1.5	0.38	0.82	1.2
90	1000	19	3.5	2.7	0.89	1.9/1.2	0.32	0.83	1.2
104	0	21	3.6	2.7	0.77	3.6/2.4	0.72	0.72	1.3
104	100	34	3.5	2.7	0.94	2.2/1.3	0.39	0.72	1.3
104	1000	39	3.4	2.7	0.98	1.9/1.1	0.31	0.72	1.3

wetting angle, the initial Ni tortuosity of about $\tau_{Ni} = 21$ increases signif icantly with time and assumes a final value of about $\tau_{Ni} = 39$. It is noted that the initial microstructure is already suffering from an inefficient electron conduction, as the tortuosity is relatively high ($\tau_{Ni} \gg 1$). The increase in tortuosity corresponds to a further and significant reduction in the effective conductivity (cf. Eq. (16)). The increase in tortuosity is most pronounced in early time, consistent with the behavior of the mean nickel diameter, but shows various discontinuities which are absent in the particle diameter curve. For the intermediate wetting angle, the tortuosity remains relatively constant with time but similarly shows a non smooth behavior which is however less pronounced. For very low wetting angle, the initially high tortuosity value drops down relatively smoothly to a value of about $\tau_{Ni} = 11$ in the final state. Therefore, the wetting angle largely influences the long term electron conduction as well.

To investigate the reaction site distribution, the l_{TPB} evolution is shown in Fig. 5(d). Interestingly, it is found that the l_{TPB} evolution is almost fully independent of the wetting angle. The l_{TPB}, initially of about 3.6 µm^{-2} decays initially relatively quickly, while at late times a value of approximately 1.9 µm^{-2} is approached. The overall reduction in TPBL is therefore about 54 percent. In Fig. 5(e), the evolution of the active part of the triple phase boundary is shown. It is found that higher wetting angles lead to a lower value of l_{ATPB}, which is caused by a higher fraction of isolated particles. The l_{ATPB} curve also features certain discontinuities which are more pronounced for large wetting angles. Similar as for the nickel tortuosity (Fig. 5(c)), although different in shape, the magnitude of the discontinuities apparently increases with increasing wetting angles. It has to be mentioned, that since it resides on a pure topological property, the detection of nickel islands is discrete in nature explaining the different shapes and locations of the discontinuities in Fig. 5(c) and (e). In this regard, please also consider the limitations of the finite sample size, as discussed in Section 4.3. It is deduced, that a good wetting of nickel on the YSZ substrate helps keeping the particles connected and therefore increases the number of available reaction sites, although the l_{TPB} seems not to be directly influenced by the wetting condition.

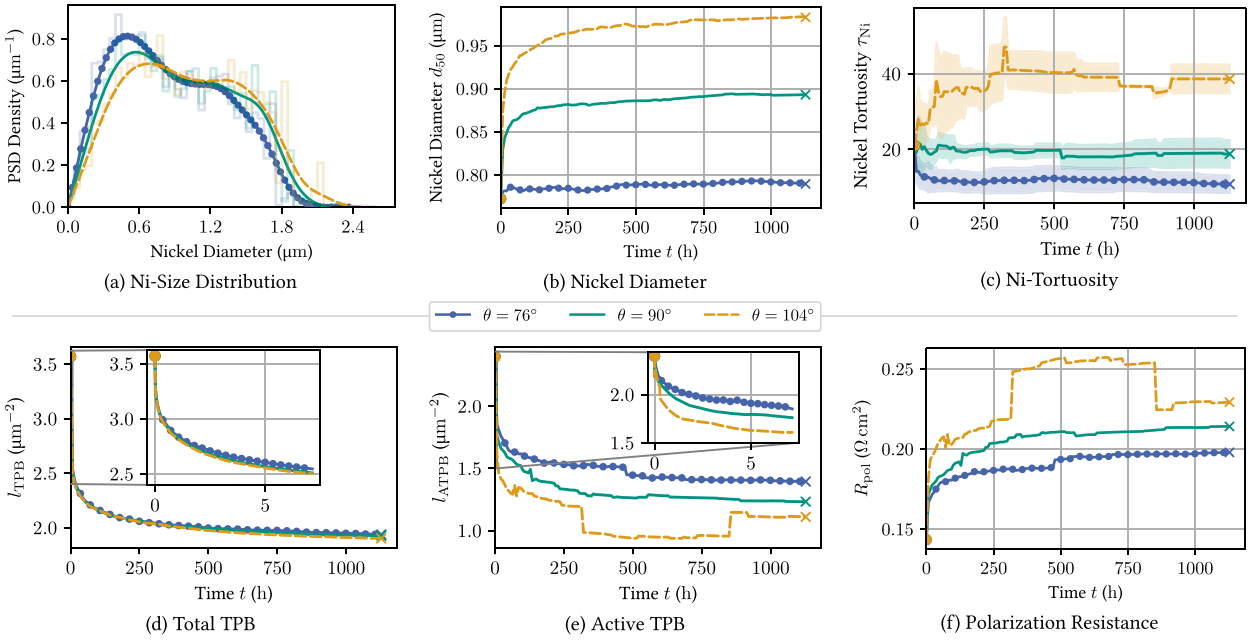

Fig. 5. Time evolution of microstructural properties in the MPF simulation for different wetting angles: Particle-size distribution of nickel (a), mean nickel diameter (b), tortuosity of nickel (c), total and active TPBL (d–e) and derived polarization resistance (f).

3.2. Polarization resistance

In this subsection, the polarization resistance of the transmission line model (Eq. (21)) is discussed. For the current choice of Z_{TLM}, one gets $\lim_{\omega\to\infty} \zeta(\omega) = 0$ and in turn the coth term in Eq. (14) tends to 1 while the prefactor tends to 0 and hence $\lim_{\omega\to\infty} Z'_{TLM}(\omega) = 0$. There fore, Eq. (21) simplifies to $R_{pol} = Z'_{TLM}(0)$. During the simulations, the volume fraction and tortuosity of YSZ remains constant and hence χ_1 remains time independent. Therefore, the variation of R_{pol} with time is solely due to a change in the triple phase boundary length l_{ATPB}.

The evolution of the polarization resistance is shown in Fig. 5(f) for a variation in wetting angle. The observed resistances are in the range $0.14 - 0.26\,\Omega\,cm^2$. All simulations show a clear increase in polarization resistance with time. This corresponds to a pronounced degradation of the anode material. The curves show a clear inverse correlation between l_{ATPB} and R_{pol} which is in line with recent experimental findings [31, Fig. 5]. The highest polarization resistance is observed for the highest wetting angle ($\theta = 104°$). The total increase of polarization resistance relative to the unannealed sample increases with wetting angle from +38% ($\theta = 76°$) over +49% ($\theta = 90°$) to +60% ($\theta = 104°$). Therefore, a good wetting on YSZ clearly improves the electrochemical performance.

4. Discussion

4.1. Additional mass transfer mechanisms

Regarding the temporal power law $t^{1/4}$ under which surface diffu sion governed phenomena develop, it is clear that coarsening of the nickel particles has to slow down as time progresses. This is due to the fact, that an arbitrarily shaped particle at doubled size requires a factor of $2^4 = 16$ more time to undergo the identical relative morphological change. A consequence of this is that the small particles in the system obtain a local equilibrium shape (a surface of constant mean curvature) relatively quickly, while the coarsening of large particles proceeds at orders of magnitude larger timescales. This likely explains the high coarsening rates observed in the simulation at early times.

Moreover, once all particles have reached such a quasi equilibrium state, the current model will not allow any further coarsening in the system. However, in the real system it may on the contrary be that additional transfer mechanisms contribute significantly at late times, even though they can be neglected at early time. This is emphasized considering the long operating times of SOFC devices of several ten thousands of hours. Therefore, while surface diffusion is likely the dominant mass transfer mechanism in the initial period of operation, additional mass transfer mechanisms may contribute to further degra dation, eventually causing the failure of the anode at late times. Mullins [59] discussed the role of evaporation condensation in comparison to surface diffusion in one of his seminal papers, as follows: *Evidently surface diffusion is initially dominant when t is small, but becomes of less relative importance as the groove develops [at late times]* and concluded that a change in the atmospheric conditions towards a less inert vapor and higher temperatures are in the favor of evaporation. Similar argu ments (*It is easy to see from the time laws [of surface and volume diffusion], that surface diffusion must dominate the initial [period of time]*) apply to volume diffusion [60].

While the current model can be easily extended for an additional contribution of volume diffusion, the action of evaporation condensation is not yet included in the model. All these additional contributions require experimental measured input parameters at oper ation conditions and thus a careful calibration. Additionally, a relevant hurdle in this regard is the computational cost associated with the long simulation times required to resolve these gradual changes of microstructure with time.

Possible additional contributions to the transport of nickel may be due to diffusion along the nickel YSZ interface or along the YSZ surface. These contributions are currently neglected due to the lack of experimental data. Please also note that based on results presented in [61], the contribution of the anode sided degradation to the total decrease in R_{pol} at operating times of several ten thousand hours might become less relevant.

4.2. Review of the transmission line model

The currently applied transmission line model is derived assuming a homogeneous distribution of each phase within the microstructure. However, the current study showed that this is not always the case since the anode consists of large pores that may lead to agglomeration

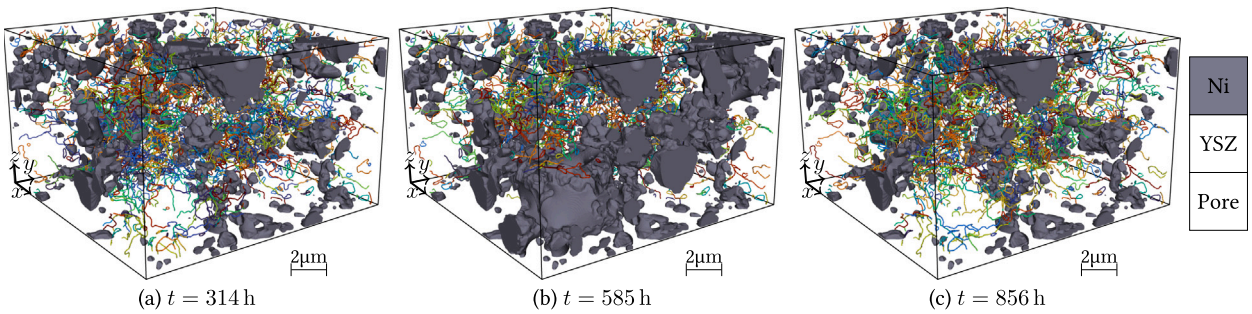

(a) $t = 314\,\mathrm{h}$ (b) $t = 585\,\mathrm{h}$ (c) $t = 856\,\mathrm{h}$

Fig. 6. Active three-phase boundary, each segment colored separately, and corresponding nickel islands (dark gray) at three different times during the simulation at $\theta = 104°$. (For interpretation of the references to color in this figure legend, the reader is referred to the web version of this article.)

of large nickel clusters. Thus, the condition that the size of structural features is much smaller than the layer thickness is not always fulfilled. This may in part limit the applicability of the herein utilized TLM. For a more realistic treatment of anodes with local variations in composition or multilayer structures, a more advanced impedance model as proposed by Dierickx et al. [62] may be a suitable choice. An alternative is to calculate the full three dimensional distribution of ionic potential following Häffelin et al. [63]. Nevertheless, both approaches increase the level of complexity. We think that the current treatment can be considered as a first estimate for the anode performance, although it may not capture all of the details required to predict the real life behavior.

4.3. Limited sample size

There are certain limitations associated with the limited size of the reconstructed volume used for the simulations. The initially high nickel tortuosities indicate that there are only few transport pathways available for the electron transport in the sample. This makes the quantity sensitive to slight microstructural changes. For the sample subject to dewetting conditions ($\theta = 104°$), this tortuosity increased significantly and in a discontinuous fashion (Fig. 5(c)). The discontinuity of the active TPBL is even more pronounced (Fig. 5(e)). To understand the corresponding reason, nickel islands and the active TPB are shown in Fig. 6 for times shortly before a distinct drop in l_{ATPB} (Fig. 6(a), $t = 314\,\mathrm{h}$), at an intermediate state (Fig. 6(b), $t = 585\,\mathrm{h}$), as well as shortly after the reverse jump (Fig. 6(c), $t = 856\,\mathrm{h}$). It can be seen, that a significant portion of nickel becomes isolated at the early event and reconnects at later time. The figure illustrates that local microstructural events may have long range effects. These effects occur because some nickel particles are sized comparable to the anode layer thickness and thus may be related to the peculiarity of the herein studied microstructure. On the macroscopic scale of cell area in the order of cm^2 ($1\,\mathrm{cm}^2$ is roughly a million times our sample area), we think that such effects are not measurable in terms of the polarization resistance as distinct jumps of significant magnitude but likely appear in the form of noise. Therefore, the local variations observed here need to be considered statistically for a macroscopic sample. The sample of the current work unfortunately does only provide limited statistical data in this regard.

5. Conclusions

In the current manuscript, nickel coarsening of FIB SEM reconstructed Ni YSZ SOFC anodes is simulated with a multiphase field model under operating conditions of 750 °C for more than 1000 h. The influence of the wettability of nickel on YSZ is discussed in detail. Thereby, a large number of different microstructural properties are calculated, including nickel diameter and particle size distributions, tortuosities and triple phase boundary lengths, as well as specific interfacial areas. The microstructural properties from the phase field simulations are used as an input for an established transmission line model (TLM) to estimate the performance of the anode as it evolves with time. Overall, the observed coarsening occurs quickly in the first few hundred hours and slows down as time progresses, which is in qualitative agreement with experimental measurements of the same material from literature. The simulations show that a low wetting of nickel is responsible for accelerated coarsening. This enhanced coarsening leads to the breakup of nickel particles and consequently to locally isolated anode regions which do not contribute to the electrochemical performance of the anode. The triple phase boundary length l_{TPB} is insusceptible to a change in the wetting conditions. However, the active TPBL can be largely reduced at low wettability of nickel on YSZ. The additional application of the TLM revealed that an increase in polarization resistance is closely linked to the observed decrease of triple phase boundary lengths. Therefore, a significant degradation of the anode material is predicted by the multiphase field model among all the different sets of parameters. Disregarding isolated nickel particles reveals an increased polarization resistance which is most pronounced in case of a low wettability of nickel.

CRediT authorship contribution statement

Paul W. Hoffrogge: Methodology, Software, Visualization, Validation, Writing original draft, Writing review & editing. **Daniel Schneider:** Methodology, Project administration, Conceptualization, Writing review & editing. **Florian Wankmüller:** Investigation, Methodology, Formal analysis, Writing original draft. **Matthias Meffert:** Investigation, Resources. **Dagmar Gerthsen:** Funding acquisition, Project administration, Supervision, Resources, Writing review & editing. **André Weber:** Funding acquisition, Project administration, Resources, Conceptualization, Supervision, Writing review & editing. **Britta Nestler:** Funding acquisition, Project administration, Conceptualization, Supervision. **Matthias Wieler:** Funding acquisition, Resources, Conceptualization.

Declaration of competing interest

The authors declare that they have no known competing financial interests or personal relationships that could have appeared to influence the work reported in this paper.

Data availability

Data will be made available on request.

Acknowledgments

Most of this work was performed on the supercomputer ForHLRII funded by the Ministry of Science, Research and the Arts Baden Württemberg and by the Federal Ministry of Education and Research. The authors acknowledge support by the state of Baden Württemberg

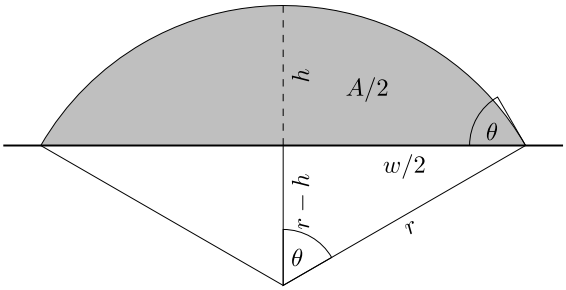

Fig. A.7. Schematical depiction of a nickel particle (gray) in equilibrium with the YSZ substrate (horizontal line).

Table A.4
Comparison of analytical and simulational droplets for $\epsilon/\Delta x = 2$.

γ_{NiYSZ} (u_E/u_l^2)	θ (°)	$2h/w$ analytical	$2h/w$ sim	$\Delta\theta$ (°)
0.5	60	0.5774	0.6165	3.3
0.75	75.52	0.7746	0.8148	2.8
1.0	90	1	1.068	3.8
1.25	104.5	1.291	1.410	4.8
1.5	120	1.732	1.770	1.1

through bwHPC. The authors gratefully acknowledge funding by the German Federal Ministry for Economic Affairs and Energy in the project KerSOLife100 (BMWi, funding nrs. 03ET6101A F) and by the German Federal Ministry of Education and Research in the project WirLeben SOFC (BMBF, funding nr. 03SF0622D). The current work was additionally funded by the Initiative and Networking Fund of the Helmholtz Association (project TwinSOC, nr. DB001840).

Appendix. Wetting angles

In the current model, the contact angles at the YSZ surface are tuned indirectly via the interfacial energies $\gamma_{\alpha\beta}$. According to Young's law, the contact angle θ is given in terms of the interfacial energies by

$$\theta = \arccos\left(\frac{\gamma_{\mathrm{PoreYSZ}} - \gamma_{\mathrm{NiYSZ}}}{\gamma_{\mathrm{NiPore}}}\right). \tag{A.1}$$

An equilibrium is achieved when the surface flux vanishes, which corresponds to a constant chemical potential and hence curvature of the surface. In two dimensions this corresponds to a spherical droplet, as depicted in Fig. A.7. The same method for validating wetting angles has been applied in our recent work [44] in the context of multiphase flow, but is recalled here to keep the document self contained. The aspect ratio h/w of the droplet is related to the angle θ by means of the equation

$$\frac{2h}{w} = \tan\frac{\theta}{2}, \tag{A.2}$$

which is found by trigonometry and the area of the droplet is equally

$$A = r^2\left(\theta - \sin\theta\cos\theta\right). \tag{A.3}$$

In order to validate the model, two dimensional simulations of an initially rectangular nickel particle, attached to a flat YSZ substrate are performed. The simulation is run for a sufficient long time such that only negligible changes are observed at late times, which corresponds to an equilibrated system.

The resulting droplet geometries are shown in addition to the the oretical shapes in Fig. A.8, by taking into account Eqs. (A.2) and (A.3) for a variety of different theoretical angles by means of varying γ_{NiYSZ} values. The results show a good agreement with the analytical solution. A quantitative comparison for the current resolution $\epsilon/\Delta x = 2$ can be found in Table A.4, where the error $\Delta\theta = 2\arctan(2h/w) - \theta$ is tabulated for different choices of γ_{NiYSZ} by taking θ according to Eq. (A.1). The accuracy of a few degree can be improved by an increased resolution of the interface, as shown in Table A.5 for a ratio of $\epsilon/\Delta x = 4$.

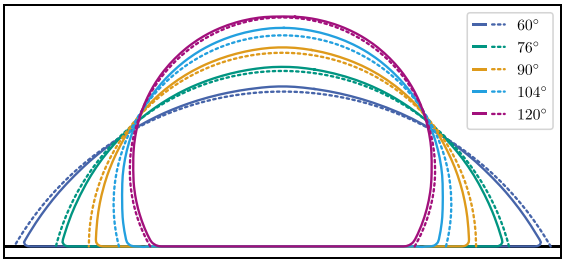

Fig. A.8. Comparison of simulational (solid) and theoretical (dashed) equilibrium droplet shapes for a resolution of $\epsilon/\Delta x = 2$.

Table A.5
Comparison of analytical and simulational droplets for $\epsilon/\Delta x = 4$.

γ_{NiYSZ} (u_E/u_l^2)	θ (°)	$2h/w$ analytical	$2h/w$ sim	$\Delta\theta$ (°)
0.5	60	0.5774	0.5852	0.68
0.75	75.52	0.7746	0.7820	0.53
1.0	90	1	1.001	0.073
1.25	104.5	1.291	1.296	0.24
1.5	120	1.732	1.709	−0.67

References

[1] A. Kirubakaran, S. Jain, R.K. Nema, A review on fuel cell technologies and power electronic interface, Renew. Sustain. Energy Rev. 13 (9) (2009) 2430–2440, http://dx.doi.org/10.1016/j.rser.2009.04.004.

[2] S.P. Jiang, S.H. Chan, A review of anode materials development in solid oxide fuel cells, J. Mater. Sci. 39 (14) (2004) 4405–4439, http://dx.doi.org/10.1023/B:JMSC.0000034135.52164.6b.

[3] H.Y. Chen, H.C. Yu, J. Scott Cronin, J.R. Wilson, S.A. Barnett, K. Thornton, Simulation of coarsening in three-phase solid oxide fuel cell anodes, J. Power Sources 196 (3) (2011) 1333–1337, http://dx.doi.org/10.1016/j.jpowsour.2010.08.010.

[4] Q. Li, L. Liang, K. Gerdes, L.Q. Chen, Phase-field modeling of three-phase electrode microstructures in solid oxide fuel cells, Appl. Phys. Lett. 101 (3) (2012) http://dx.doi.org/10.1063/1.4738230.

[5] F. Abdeljawad, B. Völker, R. Davis, R.M. McMeeking, M. Haataja, Connecting microstructural coarsening processes to electrochemical performance in solid oxide fuel cells: An integrated modeling approach, J. Power Sources 250 (2014) 319–331, http://dx.doi.org/10.1016/j.jpowsour.2013.10.121.

[6] R. Davis, F. Abdeljawad, J. Lillibridge, M. Haataja, Phase wettability and microstructural evolution in solid oxide fuel cell anode materials, Acta Mater. 78 (2014) 271–281, http://dx.doi.org/10.1016/j.actamat.2014.06.037.

[7] Z. Jiao, N. Shikazono, Simulation of Nickel Morphological and Crystal Structures Evolution in Solid Oxide Fuel Cell Anode Using Phase Field Method, J. Electrochem. Soc. 161 (5) (2014) F577–F582, http://dx.doi.org/10.1149/2.0094054jes.

[8] L. Liang, Q. Li, J. Hu, S. Lee, K. Gerdes, L.Q. Chen, Phase field modeling of microstructure evolution of electrocatalyst-infiltrated solid oxide fuel cell cathodes, J. Appl. Phys. 117 (6) (2015) http://dx.doi.org/10.1063/1.4908281.

[9] Z. Jiao, N. Shikazono, Simulation of the reduction process of solid oxide fuel cell composite anode based on phase field method, J. Power Sources 305 (2016) 10–16, http://dx.doi.org/10.1016/j.jpowsour.2015.11.061.

[10] Y. Lei, T.L. Cheng, Y.H. Wen, Phase field modeling of microstructure evolution and concomitant effective conductivity change in solid oxide fuel cell electrodes, J. Power Sources 345 (2017) 275–289, http://dx.doi.org/10.1016/j.jpowsour.2017.02.007.

[11] Z. Jiao, N. Shikazono, Prediction of Nickel Morphological Evolution in Composite Solid Oxide Fuel Cell Anode Using Modified Phase Field Model, J. Electrochem. Soc. 165 (2) (2018) F55–F63, http://dx.doi.org/10.1149/2.0681802jes.

[12] Y. Lei, T.-L. Cheng, D.S. Mebane, Y.-H. Wen, Reduced-order model for microstructure evolution prediction in the electrodes of solid oxide fuel cell with dynamic discrepancy reduced modeling, J. Power Sources 416 (January) (2019) 37–49, http://dx.doi.org/10.1016/j.jpowsour.2019.01.046.

[13] Y. Lei, T.-L. Cheng, H. Abernathy, W. Epting, T. Kalapos, G. Hackett, Y. Wen, Phase field simulation of anode microstructure evolution of solid oxide fuel cell through Ni(OH)2 diffusion, J. Power Sources 482 (July 2020) (2021) 228971, http://dx.doi.org/10.1016/j.jpowsour.2020.228971.

[14] Y. Xiang, Y. Da, N. Shikazono, Z. Jiao, Quantitative study on solid oxide fuel cell anode microstructure stability based on 3D microstructure reconstructions, J. Power Sources 477 (March) (2020) 228653, http://dx.doi.org/10.1016/j.jpowsour.2020.228653.

[15] Y. Wang, C. Wu, Q. Du, M. Ni, K. Jiao, B. Zu, Morphology and performance evolution of anode microstructure in solid oxide fuel cell: A model-based quantitative analysis, Appl. Energy Combust. Sci. 5 (November 2020) (2021) 100016, http://dx.doi.org/10.1016/j.jaecs.2020.100016.

[16] S. Yang, J. Gao, M. Trini, S. De Angelis, P.S. Jørgensen, J.R. Bowen, L. Zhang, M. Chen, Ni coarsening in Ni-yttria stabilized zirconia electrodes: Three-dimensional quantitative phase-field simulations supported by ex-situ ptychographic nano-tomography, Acta Mater. 246 (October 2022) (2023) 118708, http://dx.doi.org/10.1016/j.actamat.2023.118708.

[17] S.G. Kim, W.T. Kim, T. Suzuki, Phase-field model for binary alloys, Phys. Rev. E 60 (6) (1999) 7186–7197, http://dx.doi.org/10.1103/PhysRevE.60.7186.

[18] M. Trini, P.S. Jørgensen, A. Hauch, J.J. Bentzen, P.V. Hendriksen, M. Chen, 3D Microstructural Characterization of Ni/YSZ Electrodes Exposed to 1 Year of Electrolysis Testing, J. Electrochem. Soc. 166 (2) (2019) F158–F167, http://dx.doi.org/10.1149/2.1281902jes.

[19] F. Wankmüller, Mehrskalige Charakterisierung der Hochtemperatur-Brennstoffzelle (SOFC) (Ph.D. thesis), Karlsruhe Institute of Technology, 2022, http://dx.doi.org/10.5445/KSP/1000139659.

[20] D.J. Seol, S.Y. Hu, Z.K. Liu, L.Q. Chen, S.G. Kim, K.H. Oh, Phase-field modeling of stress-induced surface instabilities in heteroepitaxial thin films, J. Appl. Phys. 98 (4) (2005) 1–6, http://dx.doi.org/10.1063/1.1996856.

[21] L.-Q. Chen, D. Fan, Computer Simulation Model for Coupled Grain Growth and Ostwald Ripening-Application to Al2O3-ZrO2 Two-Phase Systems, J. Am. Ceram. Soc. 79 (5) (1996) 1163–1168, http://dx.doi.org/10.1111/j.1151-2916.1996.tb08568.x.

[22] S.M. Allen, J.W. Cahn, A microscopic theory for antiphase boundary motion and its application to antiphase domain coarsening, Acta Metall. 27 (6) (1979) 1085–1095, http://dx.doi.org/10.1016/0001-6160(79)90196-2.

[23] J.W. Cahn, J.E. Hilliard, Free energy of a nonuniform system. I. Interfacial free energy, J. Chem. Phys. 28 (2) (1958) 258–267, http://dx.doi.org/10.1063/1.1744102.

[24] Y.U. Wang, Computer modeling and simulation of solid-state sintering: A phase field approach, Acta Mater. 54 (4) (2006) 953–961, http://dx.doi.org/10.1016/j.actamat.2005.10.032.

[25] P.W. Hoffrogge, A. Mukherjee, E.S. Nani, P.G.K. Amos, F. Wang, D. Schneider, B. Nestler, Multiphase-field model for surface diffusion and attachment kinetics in the grand-potential framework, Phys. Rev. E 103 (3) (2021) 033307, http://dx.doi.org/10.1103/PhysRevE.103.033307.

[26] J. Nielsen, T. Klemenso, P. Blennow, Detailed impedance characterization of a well performing and durable Ni:CGO infiltrated cermet anode for metal-supported solid oxide fuel cells, J. Power Sources 219 (2012) 305–316, http://dx.doi.org/10.1016/j.jpowsour.2012.07.031.

[27] J. Nielsen, J. Hjelm, Impedance of SOFC electrodes: A review and a comprehensive case study on the impedance of LSM:YSZ cathodes, Electrochim. Acta 115 (2014) 31–45, http://dx.doi.org/10.1016/j.electacta.2013.10.053.

[28] E.-C. Shin, J. Ma, P.-A. Ahn, H.-H. Seo, D.T. Nguyen, J.S. Lee, Deconvolution of Four Transmission-Line-Model Impedances in Ni-YSZ/YSZ/LSM Solid Oxide Cells and Mechanistic Insights, Electrochim. Acta 188 (2016) 240–253, http://dx.doi.org/10.1016/j.electacta.2015.11.118.

[29] R. Mohammadi, M. Sogaard, T. Ramos, M. Ghassemi, M.B. Mogensen, Electrochemical Impedance Modeling of a Solid Oxide Fuel Cell Anode, Fuel Cells 14 (2014) 645–659, http://dx.doi.org/10.1002/fuce.201300292.

[30] S. Dierickx, J. Joos, A. Weber, E. Ivers-Tiffée, Advanced impedance modelling of Ni/8YSZ cermet anodes, Electrochim. Acta 265 (n/a) (2018) 736–750, http://dx.doi.org/10.1016/j.electacta.2017.12.029.

[31] Z. Ouyang, Y. Komatsu, A. Sciazko, J. Onishi, K. Nishimura, N. Shikazono, Operando observations of active three phase boundary of patterned nickel - Yttria stabilized zirconia electrode in solid oxide cell, J. Power Sources 529 (March) (2022) 231228, http://dx.doi.org/10.1016/j.jpowsour.2022.231228.

[32] F. Wankmüller, M. Meffert, N. Russner, A. Weber, J. Schmieg, H. Störmer, T. Dickel, P. Lupetin, N. Maier, D. Gerthsen, E. Ivers-Tiffée, Multi-scale characterization of ceramic inert-substrate-supported and co-sintered solid oxide fuel cells, J. Mater. Sci. 55 (25) (2020) 11120–11136, http://dx.doi.org/10.1007/s10853-020-04873-3.

[33] M. Cantoni, L. Holzer, Advances in 3D focused ion beam tomography, MRS Bull. 39 (2014) 354–360, http://dx.doi.org/10.1557/mrs.2014.54.

[34] M. Meffert, F. Wankmüller, H. Störmer, A. Weber, P. Lupetin, E. Ivers-Tiffée, D. Gerthsen, Optimization of Material Contrast for Efficient FIB-SEM Tomography of Solid Oxide Fuel Cells, Fuel Cells 20 (5) (2020) 580–591, http://dx.doi.org/10.1002/fuce.202000080.

[35] J. Schindelin, I. Arganda-Carreras, E. Frise, V. Kaynig, M. Longair, T. Pietzsch, S. Preibisch, C. Rueden, S. Saalfeld, B. Schmid, J.-Y. Tinevez, D.J. White, V. Hartenstein, K. Eliceiri, P. Tomancak, A. Cardona, Fiji: an open-source platform for biological-image analysis, Nature Methods 9 (2012) 676–682, http://dx.doi.org/10.1038/nmeth.2019.

[36] M. Ender, J. Joos, T. Carraro, E. Ivers-Tiffée, Quantitative Characterization of LiFePO4 Cathodes Reconstructed by FIB/SEM Tomography, J. Electrochem. Soc. 159 (7) (2012) A972—A980, http://dx.doi.org/10.1149/2.033207jes.

[37] J. Weickert, Anisotropic Diffusion in Image Processing, Teubner, 1998.

[38] J. Joos, M. Ender, I. Rotscholl, N.H. Menzler, E. Ivers-Tiffée, Quantification of double-layer Ni/YSZ fuel cell anodes from focused ion beam tomography data, Fuel Cells 246 (2014) 819–830, http://dx.doi.org/10.1016/j.jpowsour.2013.08.021.

[39] A. Choudhury, B. Nestler, Grand-potential formulation for multicomponent phase transformations combined with thin-interface asymptotics of the double-obstacle potential, Phys. Rev. E 85 (2) (2012) 021602, http://dx.doi.org/10.1103/PhysRevE.85.021602.

[40] B. Nestler, H. Garcke, B. Stinner, Multicomponent alloy solidification: Phase-field modeling and simulations, Phys. Rev. E 71 (4) (2005) 041609, http://dx.doi.org/10.1103/PhysRevE.71.041609.

[41] I. Steinbach, F. Pezzolla, A generalized field method for multiphase transformations using interface fields, Physica D 134 (4) (1999) 385–393, http://dx.doi.org/10.1016/S0167-2789(99)00129-3.

[42] P.S. Maiya, J.M. Blakely, Surface Self-Diffusion and Surface Energy of Nickel, J. Appl. Phys. 38 (2) (1967) 698–704, http://dx.doi.org/10.1063/1.1709399.

[43] M. Seiz, P. Hoffrogge, H. Hierl, A. Reiter, D. Schneider, B. Nestler, Phase-Field Simulations with the Grand Potential Approach, in: High Performance Computing in Science and Engineering '20, Springer International Publishing, Cham, 2021, pp. 561–577, http://dx.doi.org/10.1007/978-3-030-80602-6 37.

[44] M. Reder, P.W. Hoffrogge, D. Schneider, B. Nestler, A phase-field based model for coupling two-phase flow with the motion of immersed rigid bodies, Internat. J. Numer. Methods Engrg. n/a (n/a) (2002) http://dx.doi.org/10.1002/nme.6988.

[45] Y. Sun, C. Beckermann, Sharp interface tracking using the phase-field equation, J. Comput. Phys. 220 (2) (2007) 626–653, http://dx.doi.org/10.1016/j.jcp.2006.05.025.

[46] P. Haremski, L. Epple, M. Wieler, P. Lupetin, L. Klinger, E. Rabkin, M.J. Hoffmann, Grain Boundary Grooving by Surface Diffusion in Nickel Bicrystals, SSRN Electron. J. (2022) http://dx.doi.org/10.2139/ssrn.4101125.

[47] P. Haremski, L. Epple, M. Wieler, P. Lupetin, R. Thelen, M.J. Hoffmann, A Thermal Grooving Study of Relative Grain Boundary Energies of Nickel in Polycrystalline Ni and in a Ni/YSZ Anode Measured by Atomic Force Microscopy, SSRN Electron. J. 214 (2020) http://dx.doi.org/10.2139/ssrn.3730363.

[48] B. Butz, A. Lefarth, H. Störmer, A. Utz, E. Ivers-Tiffée, D. Gerthsen, Accelerated degradation of 8.5 mol% Y2O3-doped zirconia by dissolved Ni, Solid State Ion. 214 (n/a) (2012) 37–44, http://dx.doi.org/10.1016/j.ssi.2012.02.023.

[49] V. Sonn, E. Ivers-Tiffée, D. Gerthsen, Degradation in Ionic Conductivity of Ni / YSZ Anode Cermets, in: Proceedings of 8th European SOFC Forum, vol. n/a, (B1005) n/a, 2008, p. n/a.

[50] A. Utz, H. Störmer, A. Leonide, A. Weber, E. Ivers-Tiffée, Degradation and Relaxation Effects of Ni Patterned Anodes in H_2–H_2O Atmosphere, J. Electrochem. Soc. 157 (n/a) (2010) B920–B930, http://dx.doi.org/10.1149/1.3383041.

[51] A. Utz, A. Leonide, A. Weber, E. Ivers-Tiffée, Studying the CO–CO2 characteristics of SOFC anodes by means of patterned Ni anodes, J. Power Sources 196 (n/a) (2011) 7217–7224, http://dx.doi.org/10.1016/j.jpowsour.2010.10.056.

[52] J. Joos, T. Carraro, A. Weber, E. Ivers-Tiffée, Reconstruction of porous electrodes by FIB/SEM for detailed microstructure modeling, J. Power Sources 196 (17) (2011) 7302–7307, http://dx.doi.org/10.1016/j.jpowsour.2010.10.006.

[53] K. Palàgyi, A. Kuba, A 3D 6-subiteration thinning algorithm for extracting medial lines, Pattern Recognit. Lett. 19 (7) (1998) 613–627, http://dx.doi.org/10.1016/S0167-8655(98)00031-2.

[54] B. Münch, L. Holzer, Contradicting geometrical concepts in pore size analysis attained with electron microscopy and mercury intrusion, J. Am. Ceram. Soc. 91 (12) (2008) 4059–4067, http://dx.doi.org/10.1111/j.1551-2916.2008.02736.x.

[55] L. Holzer, B. Iwanschitz, T. Hocker, B. Münch, M. Prestat, D. Wiedenmann, U. Vogt, P. Holtappels, J. Sfeir, A. Mai, T. Graule, Microstructure degradation of cermet anodes for solid oxide fuel cells: Quantification of nickel grain growth in dry and in humid atmospheres, J. Power Sources 196 (3) (2011) 1279–1294, http://dx.doi.org/10.1016/j.jpowsour.2010.08.017.

[56] D. Simwonis, Nickel coarsening in annealed Ni/8YSZ anode substrates for solid oxide fuel cells, Solid State Ion. 132 (3–4) (2000) 241–251, http://dx.doi.org/10.1016/S0167-2738(00)00650-0.

[57] S.P. Jiang, Sintering behavior of Ni/Y2O3-ZrO2 cermet electrodes of solid oxide fuel cells, J. Mater. Sci. 38 (18) (2003) 3775–3782, http://dx.doi.org/10.1023/A:1025936317472.

[58] A. Faes, A. Hessler-Wyser, D. Presvytes, C.G. Vayenas, J. Van herle, Nickel-Zirconia Anode Degradation and Triple Phase Boundary Quantification from Microstructural Analysis, Fuel Cells 9 (6) (2009) 841–851, http://dx.doi.org/10.1002/fuce.200800147.

[59] W.W. Mullins, Theory of thermal grooving, J. Appl. Phys. 28 (3) (1957) 333–339, http://dx.doi.org/10.1063/1.1722742.

[60] W.W. Mullins, Grain boundary grooving by volume diffusion, Trans. Am. Inst. Min. Metall. Engineers 218 (2) (1960) 354–361.

[61] Z. Lyu, H. Li, M. Han, Z. Sun, K. Sun, Performance degradation analysis of solid oxide fuel cells using dynamic electrochemical impedance spectroscopy, J. Power Sources 538 (2022) 231569, http://dx.doi.org/10.1016/j.jpowsour.2022.231569.

[62] S. Dierickx, T. Mundloch, A. Weber, E. Ivers-Tiffée, Advanced impedance model for double-layered solid oxide fuel cell cermet anodes, J. Power Sources 415 (January) (2019) 69–82, http://dx.doi.org/10.1016/j.jpowsour.2019.01.043.

[63] A. Häffelin, J. Joos, A. Weber, E. Ivers-Tiffée, Three-Dimensional Performance Simulation of SOFC Anodes Using FIB-Tomography Reconstructions, ECS Trans. 57 (1) (2013) 2563–2572, http://dx.doi.org/10.1149/05701.2563ecst.